PAPER

Cold plasma finite element wave model for helicon waves

IOP Publishing Plasma Physics and Controlled Fusion
Plasma Phys. Control. Fusion **61** (2019) 045008 (11pp) https://doi.org/10.1088/1361-6587/aafd04

Cold plasma finite element wave model for helicon waves

C Lau[1], L A Berry[2], E F Jaeger[2] and N Bertelli[3]

[1] Oak Ridge National Laboratory, Oak Ridge, TN, United States of America
[2] XCEL Engineering, Inc., Oak Ridge, TN, United States of America
[3] Princeton Plasma Physics Laboratory, Princeton, NJ, United States of America

E-mail: lauch@ornl.gov

Received 20 September 2018, revised 30 November 2018
Accepted for publication 9 January 2019
Published 26 February 2019

Abstract

Helicon waves have been recently proposed as an off-axis current drive actuator due to their expected high current drive efficiency in the mid-radius region in high beta tokamaks. This current drive efficiency has mostly been calculated ignoring the effects of the plasma in the scrape-off-layer (SOL) in the modeling. The net core current drive efficiency will decrease if helicon power is lost to the SOL. Previous efforts to estimate the loss of helicon power in the SOL have used the hot plasma code AORSA. The large computational cost of AORSA prevents large parametric scans, so to further the understanding of helicon power loss in the SOL, a reduced finite element, full wave plasma model with effective collision frequency for collisional and Landau damping has been developed to study the helicon wave power lost to the SOL. It will be shown that the reduced finite element model (FEM) can reproduce the magnitude and trends of helicon $|E|$ field patterns and power loss in the SOL of the hot plasma AORSA model. The reduced FEM provides significant advantages over AORSA in reducing the computational time and memory requirements, and in simulating arbitrary tokamak vessel geometry. Parametric scans of antenna parallel refractive index, antenna location, minimum SOL density, SOL density gradient, and vacuum vessel geometry will be carried out to determine the dependencies of the helicon power lost to the SOL as a function of important parameters. The helicon cutoff density is shown to be an important quantity in determining helicon power lost to the SOL. Losses due to antenna loading and wave accessibility are also observed at different antenna and plasma parameters.

Keywords: helicon wave, finite element, current drive, tokamak, scrape-off-layer, DIII-D

(Some figures may appear in colour only in the online journal)

1. Introduction

For future steady-state tokamak reactor, numerous previous papers [1–10] have demonstrated that external current drive is necessary to supplement the plasma generated bootstrap current. While most of these studies have focused on using neutral beams, electron cyclotron waves, lower hybrid waves, and fast waves to drive current in tokamaks, recent studies have suggested that the helicon wave could be a promising and efficient actuator to drive non-inductive current off-axis in the mid-radius region of high beta advanced tokamaks [11, 12]. While these simulation results are encouraging, they do not include the effects of the scrape-off-layer (SOL). AORSA [13], a hot plasma, full wave model that is valid to all order of Larmor radius and arbitrary cyclotron harmonic, has demonstrated good agreement with previous ray tracing [12] when the SOL is not included in the model [14]. When the SOL is included in the AORSA model, helicon power is lost to the SOL and reduces the net core current drive efficiency. At low SOL densities, plasma-antenna coupling can cause significant helicon power loss to the SOL. At high SOL densities, strong helicon $|E|$ fields, possibly a standing wave, form in the SOL, causing increased SOL losses. There is an optimized SOL density that minimizes the helicon power losses to the SOL.

While AORSA can calculate the power loss to the SOL using the full hot plasma dielectric tensor, it is not suitable for large, parametric scans because it is too computationally intensive. A reduced computational model will be preferred for large parametric scans, especially since the full hot plasma dielectric tensor may not be necessary for helicon wave physics in the SOL. While ray tracing models are computationally inexpensive, ray tracing is too simplified and cannot calculate the strong $|E|$ fields and standing wave in the SOL [14]. AORSA also currently can solve the helicon wave problem only in a rectangular domain and cannot simulate realistic tokamak vessel geometry. Given that possible standing waves can be sensitive to vacuum vessel geometry [15], realistic geometry could greatly affect the results.

A reduced 2D axisymmetric finite element plasma model that can resolve arbitrary tokamak geometry has therefore been developed to study helicon power loss to the SOL. The model uses the Stix cold plasma dielectric tensor with a modified effective collision frequency [16] that approximates the power absorption from collisional and Landau damping. No other warm or hot plasma features are modeled. While this reduced finite element model (FEM) may appear to be simple, it can reproduce the trends for helicon electric field, $|E|$, and power absorbed in the core and SOL of hot plasma AORSA simulations. The reduced FEM can furthermore be simulated in a few minutes on a HP Z800 desktop workstation.

This paper is structured as follows. section 2 introduces and describes the reduced FEM. Section 3 validates the numerical model. Comparison of the reduced FEM between previous calculations using GENRAY and AORSA show good agreement in both trend and magnitude of the $|E|$ and SOL power absorption for a DIII-D integrated scenario. The inclusion of the Landau damping term in the effective collision frequency is shown to be crucial for this agreement. Section 4 shows the results of the reduced FEM for a range of plasma parameters such as SOL density and temperatures. The importance of the fast wave cutoff density is highlighted here in understanding SOL losses. Section 5 shows the results of the reduced FEM for a range of antenna parameters such as the antenna location and antenna refractive index. Antenna loading and wave accessibility effects on the SOL loss are observed here. Section 6 presents the effect of different vacuum vessel geometries on the helicon wave physics. A larger volume in the SOL is observed to increase SOL losses. Section 7 concludes the paper.

2. Finite element model

Previous publications have used FEM, such as the finite element package COMSOL [17], to solve a vector wave equation with a plasma dielectric tensor for ion cyclotron heating [18–20] and lower hybrid current drive [21–23] on tokamaks. Solution with finite elements in real space usually limits the plasma dielectric tensor to the standard 3×3 Stix cold plasma tensor [24]. The full hot plasma dielectric tensor is a non-local tensor and cannot be solved with standard finite element methods. It usually requires numerically intensive spectral methods to solve, although it has proven to be possible to include some hot plasma effects for lower hybrid waves in a FEM [21]. This method, however, still requires fast Fourier transforms and is computationally intensive. It is also unclear how to extend the theoretical treatment to fast waves and helicon waves. Given that the computationally intensive hot plasma code AORSA can already model these hot plasma effects through the use of a spectral method [13], one of the main goals of this FEM is to reduce the computational complexity by having a local plasma dielectric tensor in real space while maintaining enough physics to better understand the helicon power absorption in the SOL.

The equation solved in this paper is shown in equation (1) where E is the helicon wave electric field, ω is helicon wave angular frequency, $\vec{\vec{\varepsilon}}$ is the plasma dielectric tensor, and $\vec{J}_{\text{ext}}$ is an externally specified helicon wave current density

$$\nabla \times (\nabla \times \vec{E}) - \frac{\omega^2}{c^2}(\vec{\vec{\varepsilon}} \cdot \vec{E}) = -\mathrm{i}\omega\mu_0 \vec{J}_{\text{ext}}. \tag{1}$$

COMSOL is used to solve this equation in 2D axisymmetric geometry. A triangular mesh with quadratic shape functions and a maximum mesh element size of 3 mm are used. Based on previous calculations using the dispersion relation [25] in the AORSA model, a maximum mesh element size of 3 mm is sufficient to resolve the helicon wave, but it is not sufficient to resolve the slow wave. Even in 2D, the short wavelength of the slow wave cannot be resolved in this paper with the current computational resources. In a previous [14], a 1D AORSA simulation with enough spatial resolution to resolve the slow wave in the SOL did not show any slow wave oscillatory behavior, perhaps indicating that the slow wave is not that important in this problem.

The electric field and external current density are assumed to be a harmonic mode with fixed toroidal mode number, n_φ. The external current density is imposed normal to the equilibrium magnetic field. This is shown in equation (2). n_φ is chosen by the desired parallel refractive index of the helicon antenna, $n_{||}$, where $n_{||} = cn_\varphi B_\varphi/\omega BR$. B_φ is the toroidal magnetic field, B is the total magnetic field, and R is the major radius. While all the electromagnetic and plasma parameters are a function of only R and z (vertical location), the model does solve for all vectors in all three-dimensions of R, z, and φ (aximuthal coordinate)

$$\begin{aligned} &\vec{E}(R,\ \varphi,\ z) = \vec{E}(R, z)\mathrm{e}^{\mathrm{i}n_\varphi\varphi} \\ &\text{and } \vec{J}_{\text{ext}}(R,\ \varphi,\ z) = \vec{J}_{\text{ext}}(R, z)\mathrm{e}^{\mathrm{i}n_\varphi\varphi}. \end{aligned} \tag{2}$$

The model presented here uses the Stix cold plasma tensor, which is shown in equation (3) using the standard S, D, and P definitions for sum, difference, and plasma [24]. S, D, and P are a function of helicon frequency, cyclotron frequency, and plasma frequency. $\vec{\vec{R}}$ is a rotation matrix that is used to transform the magnetic field coordinate system of the Stix plasma tensor from a slab plasma to an axisymmetric toroidal plasma. Any arbitrary axisymmetric magnetic field vector can therefore be incorporated in this simulation

through modification of the $\vec{\vec{R}}$ matrix

$$\vec{\vec{\varepsilon}} = \vec{\vec{R}} \cdot \begin{bmatrix} S & -iD & 0 \\ iD & S & 0 \\ 0 & 0 & P \end{bmatrix} \cdot \vec{\vec{R}}^T. \quad (3)$$

One major difference between this model and the standard Stix cold plasma tensor used in many previous publications [18–20] is the inclusion of collisional and Landau damping effects by replacing the mass term in the plasma and cyclotron frequency of S, D, and P in $\vec{\vec{\varepsilon}}$ with an effective mass term [24]. The definition of the effective mass is given in equation (4) where m_j is the mass of species j, and v_j is the specified collision frequency of species j

$$m_{\text{eff}} = m_j\left(1 + i\frac{v_j}{\omega}\right). \quad (4)$$

The normalized effective electron collision frequency, υ_e/ω, is shown in equation (5) as the sum of a collisional damping, the first term of the right-hand side (RHS) of equation (5), and electron Landau damping, the second term in the RHS of equation (5)

$$\frac{v_e}{\omega} = \frac{\upsilon}{\omega} * (\rho > 1) + 2\sqrt{\pi}\frac{\omega^3}{k_{||j}^3 v_{\text{th}j}^3} e^{\frac{-\omega^2}{k_{||j}^2 v_{\text{th}j}^2}} \quad (5)$$

υ_i/ω is assumed to be $\nu/\omega\ ^*\ (\rho > 1)$. The collisional damping is assumed to exist only in the SOL in this simulation. This collisional damping is not designed to be a first principles description, but as a proxy for any SOL damping physical mechanisms. This allows for a numerical study of the power loss of the helicon wave in the SOL. ρ is the square root of the normalized toroidal flux and is defined to be 1 at the last closed flux surface (LCFS). The SOL losses quoted in this paper are therefore estimates and are used to understand trends and not to quantitatively predict SOL losses.

Assuming the electrons are a normal distribution and $k_{||}v_{\text{th}}/\omega \ll 1$, the effects of electron Landau damping on the power absorption can be equated to an effective collision frequency described by the second term in the RHS of equation (5). The derivation of the electron Landau damping term is discussed in [16], and depends on the thermal velocity, v_{th}, and parallel wavenumber, $k_{||}$. The parallel wavenumber is set by the desired antenna spectrum and assumed equal to $n_\varphi B_\varphi/BR$ in this paper.

The modified Stix plasma tensor depends on electron density, electron temperature, and magnetic field. Temperature is necessary because of the thermal velocity in the electron Landau damping term. These inputs have been taken from experimental DIII-D discharges and modeled integrated scenarios. Standard EFIT magnetic equilibrium is used for magnetic field inputs. Density and temperature within the LCFS are provided from Thomson scattering for DIII-D discharges or by modeled results for a projected integrated scenario.

The SOL density profile is not provided in these scenarios and is modeled as an exponential decay, shown in equation (6) below where $n_{\min}$ and L are the minimum electron density and the SOL decay length, respectively. $n_{\min}$ and L are variable inputs in this paper and provide convenient parameters to understanding the SOL losses as a function of different density profiles

$$n_e = n_{\min} + [(n_e(\rho = 1) - n_{\min}] * e^{-\frac{\rho-1}{L}}. \quad (6)$$

The SOL temperature model is also modeled as an exponential decay. Scans of the SOL temperature, however, minimally modifies the reduced finite element solution because the temperature is too low for any significant Landau damping. This scan is therefore not shown in this paper.

$\mathscr{J}_{\text{ext}}$ is modeled as a normal distribution in both ρ and z where ant_ρ and ant_z are the antenna radial and vertical location, and $\text{ant\_}w_\rho$ and $\text{ant\_}w_z$ are the radial and poloidal decay lengths. Other possible shapes for such as cosine or uniform function were tried for $\mathscr{J}_{\text{ext}}$, and while they made some small changes quantitatively, it did not change the trends shown in this paper. The antenna current density is designed to be curved and follow a flux function radially. It therefore has current in both radial and vertical direction that is angled with respect to the flux surface. The magnitude of the external current density is shown in equation (7)

$$\mathscr{J}_{\text{ext}}(R, z) = e^{-\left(\frac{\rho-\text{ant}_\rho}{\text{ant\_}w_\rho}\right)^2} * e^{-\left(\frac{z-\text{ant}_z}{\text{ant\_}w_z}\right)^2}. \quad (7)$$

This choice is identical to the external current density in AORSA, allowing for comparison between the two models [14]. ant_ρ, and ant_z are variable inputs in this paper $\text{ant\_}w_\rho$ and $\text{ant\_}w_z$ are not varied in this paper and assume to equal 0.045 and 0.1875 in this paper. This was mostly done to match previous AORSA simulation results, which for numerical reasons, were sensitive to these input parameters.

The key metric used in this paper, the fractional power loss in the SOL, f_{SOL}, is defined in equation (8) as the ratio of the integrated electric power density in the SOL over the total integrated electric power density. J is the plasma current density, E is the helicon electric field and the integral is evaluated over the volume of the tokamak geometry. f_{SOL} will be used to determine the effect of SOL on the helicon wave physics, and demonstrate the validity of the reduced FEM

$$f_{\text{SOL}} = \frac{\int (J \cdot E) * (\rho > 1) dV}{(J \cdot E) dV}. \quad (8)$$

3. Verification of the FEM

The reduced FEM is compared with AORSA and GENRAY, which have been previously used to model helicon waves [12, 14]. Core electron density, core electron temperature, and magnetic field inputs to the reduced finite element simulation are from a high beta integrated DIII-D scenario [26] with substantial electron cyclotron and neutral beam heating, so that the normalized beta is about 5% and central density of $6 \times 10^{19}\,\text{m}^{-3}$. These profiles are shown in figure 1 for the density profile (red solid line), temperature profile (blue dashed line), and Z_{eff} profile (green dotted line). The antenna frequency is 476 MHz and 1 MW power is assumed at the

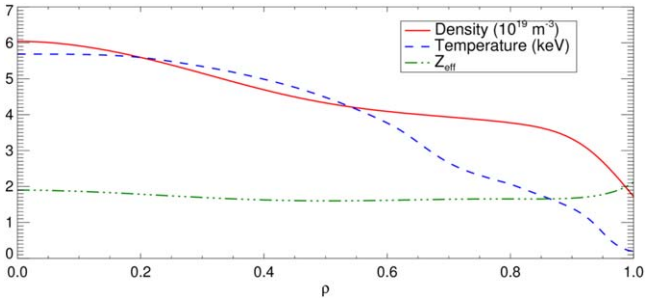

Figure 1. Density (red solid line), temperature (blue dashed line), and Z_{eff} (green dotted–dashed line) profiles as a function of ρ is shown for the high beta integrated DIII-D scenario.

launch location. These parameters are chosen to compare with previous AORSA simulations and are the design point for a helicon antenna on DIII-D [14].

Comparison of the $|E|$ profile between the reduced FEM, AORSA, and GENRAY is shown in figure 2 for four different n_{min}. Figures 2(a)–(d) show the results of the FEM for $n_{\text{min}} = 2 \times 10^{18}\,\text{m}^{-3}$, $3 \times 10^{18}\,\text{m}^{-3}$, $4 \times 10^{18}\,\text{m}^{-3}$, and $5 \times 10^{18}\ \text{m}^{-3}$. $L = 0.08\,\text{m}$, $\text{ant}_z = 0.45\,\text{m}$, $\text{ant}_\rho = 1.3$, and $n_{||} = 4$. Figures 2(e)–(h) shows the corresponding results of these four n_{min} values for the AORSA model. GENRAY ray tracing [27] is also shown by the black line. $\rho = 0.2$, 0.4, 0.6, 0.8, and 1 are shown by the gray lines. In figure 3, comparison of the power absorption profile between the reduced FEM and AORSA is shown. Figures 3(a)–(d) show the results of the reduced FEM for $n_{\text{min}} = 2 \times 10^{18}\,\text{m}^{-3}$, $3 \times 10^{18}\,\text{m}^{-3}$, $4 \times 10^{18}\,\text{m}^{-3}$, and $5 \times 10^{18}\,\text{m}^{-3}$. Figures 3(e)–(h) shows the corresponding results with these four values of n_{min} for the AORSA model.

GENRAY, AORSA, and the reduced FEM agree reasonably well for most regions within the LCFS, as GENRAY ray approximately overlaps both the $|E|$ field in the AORSA and reduced FEM. The width of the $|E|$ field beam inside the LCFS is also similar between AORSA and the FEM. Both AORSA and the reduced FEM show that the core power absorption is predominantly in the mid-radius region ($0.3 < \rho < 0.7$ in this paper).

One difference is that the $|E|$ field of the FEM in the core region ($\rho < 0.7$ in this paper) does differ from both GENRAY and AORSA models. The reduced FEM $|E|$ does appear to be slightly above the GENRAY ray. This is somewhat surprising given the agreement between GENRAY and AORSA. The reason for the discrepancy is unclear, but it appears sufficient to understand the trends in the SOL absorption, so it is not explored further here.

For the $|E|$ fields in the SOL, AORSA and reduced FEM show similar magnitude and trends with increasing n_{min}. At small n_{min}, the $|E|$ field in the SOL is dominated by the specified antenna current density for both models. As n_{min} is increased, AORSA and reduced FEM both show a strong structure in the upper right corner of the simulation. The $|E|$ field in the structure increases with increasing n_{min}. The reduced FEM additionally shows significant $|E|$ structure in the bottom right corner that are absent in the AORSA solution. One possibility to resolve the differences between the reduced FEM and AORSA is that AORSA does require numerical damping at high perpendicular wavenumbers to prevent numerical pollution. The reduced FEM does not include numerical damping at high perpendicular wavenumbers. This numerical damping may strongly diminish the $|E|$ in the SOL for structures with a high perpendicular wavenumber and may explain the appearance of short wavelength $|E|$ structure in bottom right corner of the reduced FEM where no such structure is observed in the AORSA simulations. If this is the explanation for the differences in the $|E|$ of the two models in the SOL, the reduced finite element solution should be more accurate in the SOL.

The use of the Landau damping term in the effective collision frequency can improve the agreement between AORSA and the reduced FEM. Figure 4(a) shows υ_e/ω in equation (5) for the DIII-D parameters in this paper. Figure 4(b) shows the value of $k_{||}v_{\text{th}}/\omega$. Figures 4(c) and (d) show the reduced FEM $|E|$ results with and without the effective Landau damping for $n_{\text{min}} = 3 \times 10^{18}\,\text{m}^{-3}$ case. A constant $\upsilon_e/\omega = 0.01$ is assumed in the core to reduce numerical noise. The black line shows the GENRAY result. With the effective Landau damping term, the helicon $|E|$ field appear to be similar to the AORSA solution in figure 2. The $|E|$ fields in the SOL with Landau damping are also much smaller and reasonable compared to the $|E|$ fields in the SOL without Landau damping. It should be noted that in principle, there is an arbitrary 2D υ_e/ω profile that will likely compare more favorably to the $|E|$ fields of AORSA. However, it is unclear how this υ_e/ω profiles changes with different plasma and antenna parameters. The use of this Landau damping term in the collision frequency gives a simple and somewhat physically realistic mechanism for core power absorption of the helicon waves.

This good agreement between the two models may be somewhat surprising. AORSA solves the same vector wave equation shown in equation (1) as the reduced FEM, but $\overleftrightarrow{\varepsilon}$ contains the full hot plasma dielectric tensor in AORSA. In the reduced FEM, $\overleftrightarrow{\varepsilon}$ is approximated with a cold plasma tensor supplemented with an effective collision frequency for collisional and Landau damping. For the helicon current drive scenarios examined in this paper, this approximation for $\overleftrightarrow{\varepsilon}$ may be acceptable. Previous GENRAY modeling has shown that using either the cold or hot plasma dispersion relation results in similar ray trajectories [12]. The cold plasma dielectric tensor may therefore be valid for helicon wave propagation at these densities and temperatures. The scenario is also designed to strongly damp through electron Landau damping in the mid-radius region [12]. Other effects such as transit time magnetic pumping and cyclotron resonant damping can be ignored. Inclusion of Landau damping as the only hot plasma effect is sufficient. The effective Landau damping term in equation (5) is also valid only when $k_{||}v_{\text{th}}/\omega \ll 1$. This is shown in figure 4(b) where $k_{||}v_{\text{th}}/\omega$ can be much smaller than 1 or as high as 0.8 in the core. For low temperatures in the SOL, this assumption is true. It may be possibly valid in the edge of the plasma ($\rho > 0.7$ in this paper), somewhat questionable in the mid-radius region, and likely questionable in the core of the plasma. This assumption

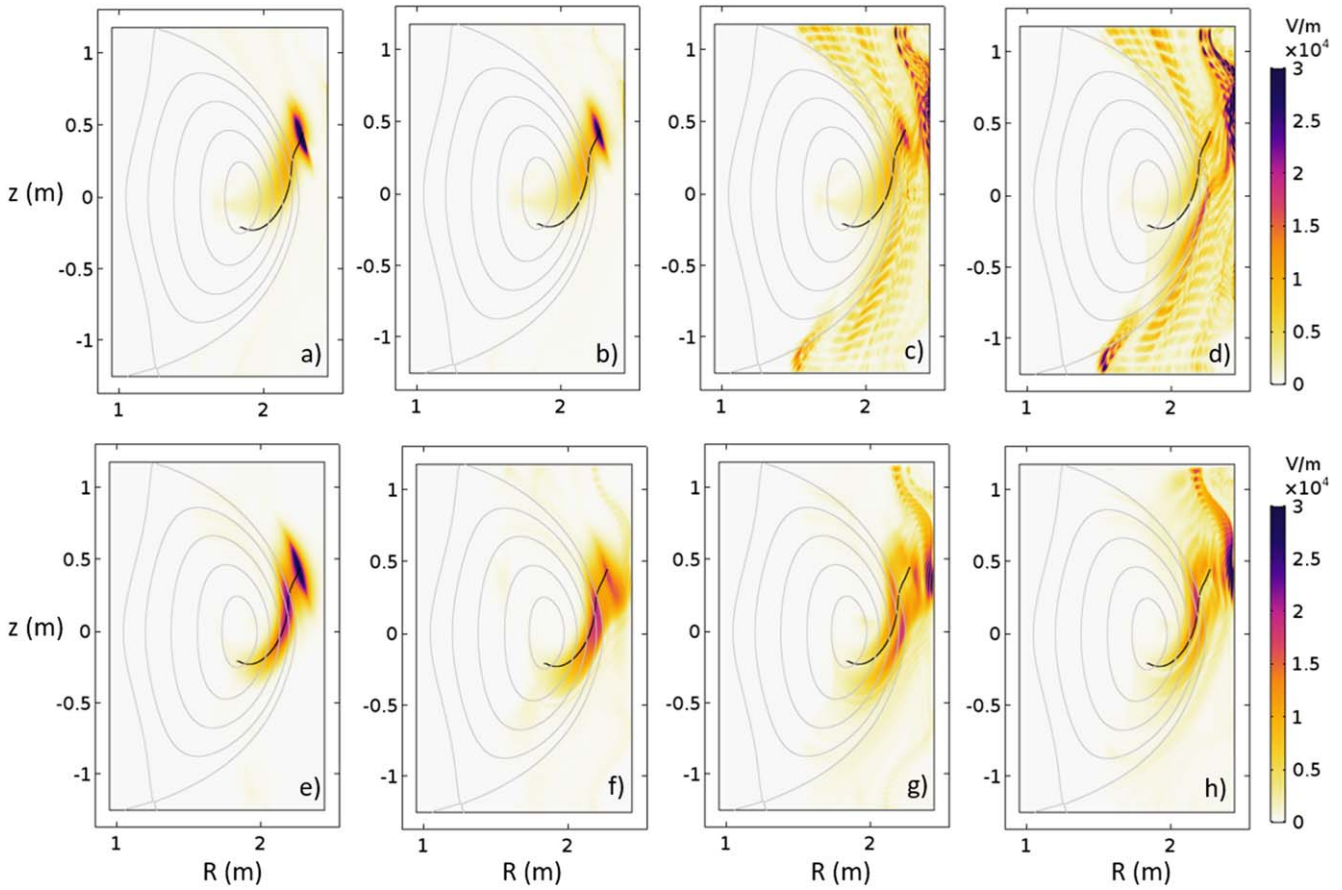

Figure 2. (a)–(d) The $|E|$ fields from FEM is shown for $n_{\min} = 2 \times 10^{18}\,\mathrm{m}^{-3}$, $3 \times 10^{18}\,\mathrm{m}^{-3}$, $4 \times 10^{18}\,\mathrm{m}^{-3}$, and $5 \times 10^{18}\,\mathrm{m}^{-3}$. (e)–(h) The $|E|$ fields from AORSA is shown for $n_{\min} = 2 \times 10^{18}\,\mathrm{m}^{-3}$, $3 \times 10^{18}\,\mathrm{m}^{-3}$, $4 \times 10^{18}\,\mathrm{m}^{-3}$, and $5 \times 10^{18}\,\mathrm{m}^{-3}$. GENRAY ray tracing is shown by the black line in (a)–(h). $L = 0.08$ m, $\upsilon_e/\omega = 0.01$, $\mathrm{ant}_z = 0.45$ m, $\mathrm{ant}_\rho = 1.3$, frequency $= 476$ MHz, and $n_{||} = 4$ for this figure.

may explain why the $|E|$ field in the reduced FEM does not agree in the core plasma with AORSA or GENRAY. Given that the Landau damping occurs mostly in the mid-radius region and not the core plasma, the assumption may be somewhat satisfied in this scenario, and perhaps is another reason for the good agreement between the two models within the LCFS.

To more quantitatively compare the two models, figure 5 shows f_{SOL} as a function of $n_{\min}$ for AORSA (blue squares) and reduced FEM at $n_{||} = 4$ (blue solid line). The trends of f_{SOL} are similar between the reduced finite element and AORSA model. Both models show high SOL power absorption at low and high $n_{\min}$. At $n_{\min} \approx 3$–$4 \times 10^{18}\,\mathrm{m}^{-3}$, the SOL power absorption is minimized. For $n_{\min} > 3 \times 10^{18}\,\mathrm{m}^{-3}$, the magnitude of f_{SOL} agrees reasonably well between the two models. For $n_{\min} < 3 \times 10^{18}\,\mathrm{m}^{-3}$, f_{SOL} in the reduced FEM is significantly higher than AORSA. While it is unclear why there is such a difference at smaller $n_{\min}$, a 5% change of $n_{||}$ for the reduced FEM (red dashed line) gives good agreement between the two models for a full range of $n_{\min}$. This is an interesting result, and further exploration is needed. The helicon wave cutoff (right-hand cutoff) density is also shown by the colored dashed vertical lines. The cutoff density [28, 29] depends on $n_{||}$ and ω, as shown in equation (9):

$$n_{\mathrm{cutoff}}(m^{-3}) = 3.45 \times 10^{14} B_T \left(\frac{\omega}{2\pi \times 10^6} + \frac{15.2}{\mu} B_T \right) (n_{||}^2 - 1), \quad (9)$$

in which we assume the ion charge $Z = 1$ and μ is the ion mass in units of proton masses (e.g. for deuterium, $\mu = 2$), B_T is the local magnetic field in T and $\omega \ll \omega_{ce}$.

For this paper that focuses on understanding the trends in the power absorption profile of the helicon waves in tokamak plasmas, the agreement between reduced FEM and AORSA is sufficient. One significant advantage of the reduced FEM is that each helicon wave simulation can be solved in a few minutes on a modern workstation. Each AORSA simulation of helicon waves require approximately 10^4–10^5 CPU hours on a large supercomputing cluster as well as significant queue waiting time. Given the reduced computational cost and turnaround time for each simulation, large parametric scans of various parameters can be achieved. Examples of these parametric scans are shown in sections 4–6.

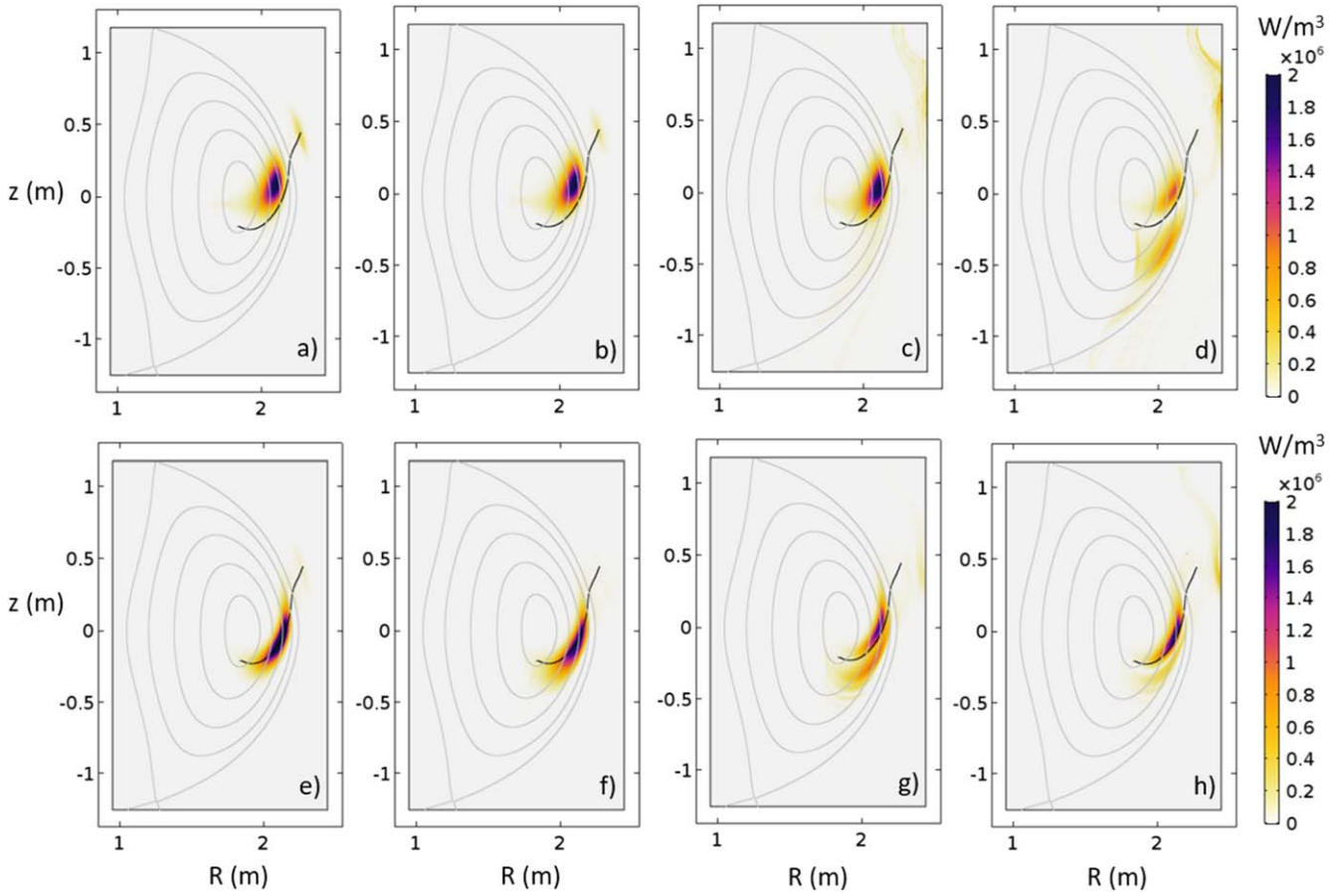

Figure 3. (a)–(d) The power absorption profile from FEM is shown for $n_{\min} = 2 \times 10^{18}\,\mathrm{m}^{-3}$, $3 \times 10^{18}\,\mathrm{m}^{-3}$, $4 \times 10^{18}\,\mathrm{m}^{-3}$, and $5 \times 10^{18}\,\mathrm{m}^{-3}$. (e)–(h) The power absorption profile from AORSA is shown for $n_{\min} = 2 \times 10^{18}\,\mathrm{m}^{-3}$, $3 \times 10^{18}\,\mathrm{m}^{-3}$, $4 \times 10^{18}\,\mathrm{m}^{-3}$, and $5 \times 10^{18}\,\mathrm{m}^{-3}$. $L = 0.08$ m, $v_e/\omega = 0.01$, $\mathrm{ant}_z = 0.45$ m, $\mathrm{ant}_\rho = 1.3$, frequency $= 476$ MHz, and $n_{||} = 4$ for this figure.

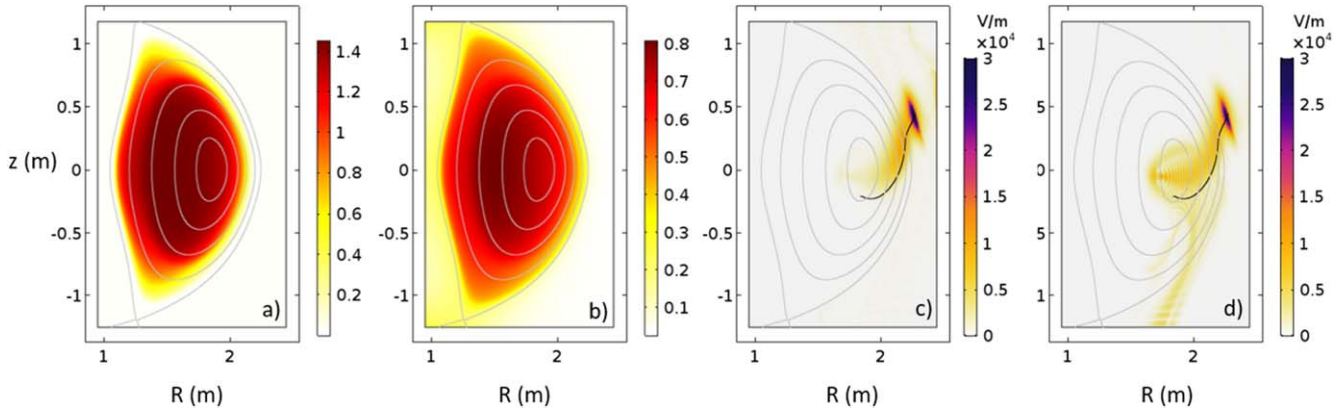

Figure 4. (a) v_e/ω using equation (5) is shown as a function of R and z. (b) $k_{||}v_{\mathrm{th}}/\omega$ is shown as a function of R and z. (c) The $|E|$ field pattern using v_e/ω from equation (5). (d) The $|E|$ field pattern using $v_e/\omega = 0.01$, $L = 0.08$ m, $n_{\min} = 3 \times 10^{18}\,\mathrm{m}^{-3}$, $\mathrm{ant}_z = 0.45$ m, $\mathrm{ant}_\rho = 1.3$, frequency $= 476$ MHz, and $n_{||} = 4$ for this figure.

4. Parametric scans of various SOL parameters

This section shows how the SOL power loss, f_{SOL}, varies with various SOL parameters, such as the minimum SOL density, SOL density gradient, and the SOL collision frequency. When not specified, the reduced FEM simulations starting from this section also use $L = 0.05$ m and $n_{||} = 3$. The central magnetic field is 1.5 T. These are more realistic parameters [14, 30] that could not be chosen due to the computational limits of the AORSA simulations in the previous section.

Because of the lack of understanding of the physical mechanisms for helicon power loss in the SOL, a SOL collision frequency is used as a knob to understand possible SOL losses. Figure 6 shows f_{SOL} as a function of ν/ω for three

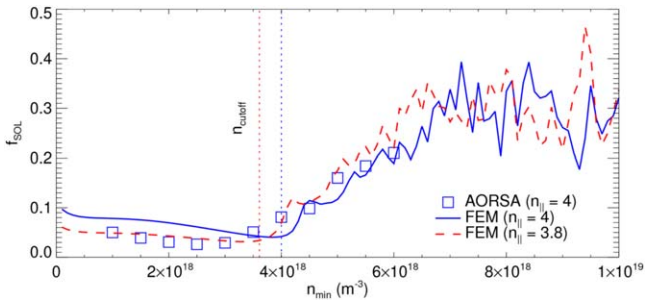

Figure 5. Comparison of reduced FEM (blue solid line) versus AORSA (blue square) for $n_{||} = 4$. Quantitative agreement is reasonable. It should be noted that the reduced FEM solution is relatively sensitive to the value of $n_{||}$, and that even better quantitative agreement can be achieved for a small 5% change in $n_{||}$ ($n_{||} = 3.8$ in the red long-dashed line) in the COMSOL model. The helicon wave cutoff density is shown in the colored short-dashed line. $L = 0.08$ m, $\upsilon_e/\omega = 0.01$, frequency $= 476$ MHz, $\text{ant}_z = 0.45$ m, and $\text{ant}_\rho = 1.3$ for this figure.

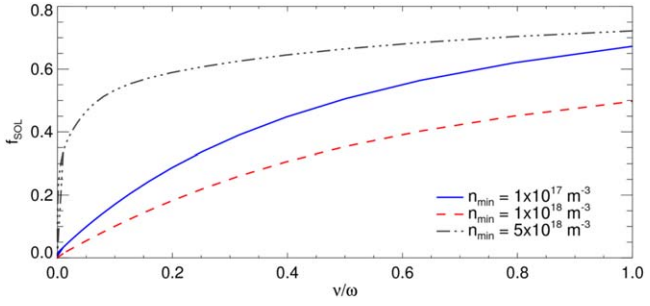

Figure 6. f_{SOL} is shown for $n_{\text{min}} = 1 \times 10^{17}$, 1×10^{18}, and 5×10^{18} m^{-3} as a function of ν/ω ranging from 0 to 1. $L = 0.05$ m, $\text{ant}_z = 0.45$ m, $\text{ant}_\rho = 1.3$, frequency $= 476$ MHz, and $n_{||} = 3$ for this figure.

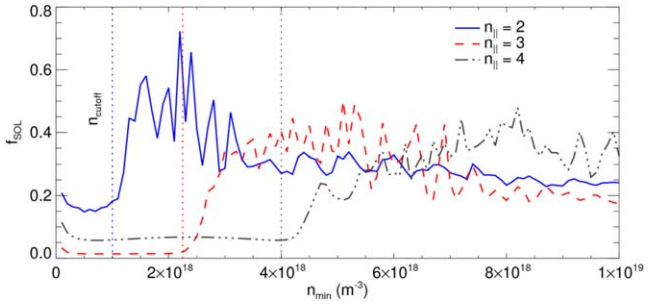

Figure 7. f_{SOL} is shown for $n_{||} = 2$, 3 and 4 as a function of n_{min} ranging from 0 to 1×10^{19} m^{-3}. $L = 0.05$ m, $\text{ant}_z = 0.45$ m, $\text{ant}_\rho = 1.3$, frequency $= 476$ MHz and $\upsilon_e/\omega = 0.01$ for this figure.

different n_{min}. f_{SOL} can vary widely depending on ν/ω. As the SOL collision frequency is increased, f_{SOL} increases accordingly. Given the uncertainty in the value of ν/ω or understanding realistic physical mechanisms for SOL loss, it is clear the quantitative value of f_{SOL} is difficult to obtain with such a simple model. However, trends in f_{SOL} with various parameters can still improve physics understanding. ν/ω is assumed to be 0.01 here, similar to previous papers [14].

One of the important results of this section is the importance of the helicon fast wave cutoff in the reduced

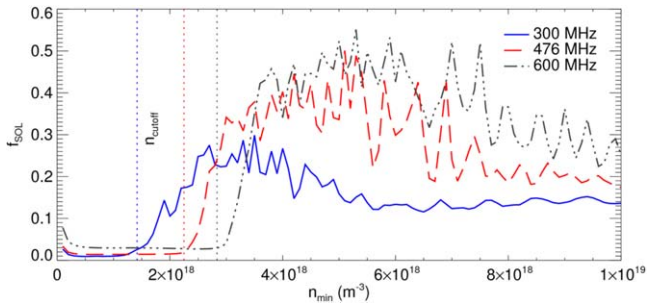

Figure 8. f_{SOL} is shown for antenna frequency of 300, 476, and 600 MHz as a function of n_{min} ranging from 0 to 1×10^{19} m^{-3}. $L = 0.05$ m, $\text{ant}_z = 0.45$ m, $\text{ant}_\rho = 1.3$, $n_{||} = 3$, and $\upsilon_e/\omega = 0.01$ for this figure.

FEM simulations. f_{SOL} has substantially different behavior when $n_{\text{min}} < n_{\text{cutoff}}$ versus when $n_{\text{min}} > n_{\text{cutoff}}$. Figure 7 highlights how f_{SOL} varies with n_{min} at three different fixed $n_{||}$. $n_{\text{cutoff}} \propto n_{||}^2$, so the cutoff density occurs at different density values for different $n_{||}$. When $n_{\text{min}} < n_{\text{cutoff}}$, the SOL losses are relatively low. For most of these n_{min} values, f_{SOL} is relatively constant, although it does increase for the lowest values of n_{min}. When $n_{\text{min}} > n_{\text{cutoff}}$, the SOL losses increase suddenly and substantially. This is similar to what was observed in figures 3 and 5.

When $n_{\text{min}} > n_{\text{cutoff}}$, the SOL losses also seem to have oscillatory behavior. The exact physical mechanism for this is unclear; however, it is not due to the slow wave since these simulations cannot resolve the slow wave. It may possible be due to cavity-like modes of the fast wave. Previous publications [31, 32] have possibly indicated that the fast wave could produce standing wave structure depending on the number of wavelengths that fit into the SOL. This is outside the scope of this paper and further investigation will be required.

Figure 8 highlights how f_{SOL} varies with n_{min} at three different fixed frequencies. $n_{\text{cutoff}} \propto \omega$, so the cutoff density occurs at different density values for different frequencies. A similar trend is observed here where for $n_{\text{min}} < n_{\text{cutoff}}$, f_{SOL} is low and constant except for the lowest n_{min}. For $n_{\text{min}} > n_{\text{cutoff}}$, the SOL losses increase suddenly and substantially. n_{min} should therefore be kept sufficiently low to avoid helicon power being lost to the SOL. If n_{min} is too low, however, SOL losses increase again, likely due to evanescent loading. This is discussed in more detail in section 5.

The density gradient, L, is also an important parameter in understanding helicon power losses. Figure 9 shows how f_{SOL} varies with L for three different n_{min}. When L is large, f_{SOL} approaches a negligible value if $n_{\text{min}} > n_{\text{cutoff}}$ If $n_{\text{min}} > n_{\text{cutoff}}$, f_{SOL} is still significant. When L is small, f_{SOL} increases substantially. This is likely due to evanescent loading, as the fast wave is cutoff at low densities. It is worth pointing out that the minimum SOL density, n_{min}, is likely less than the cutoff density based on experimental measurements [30], so the SOL losses will likely be small for realistic SOL density profiles in experiments. L can range from 0.02 to 0.08 in DIII-D [30], however, so a wide range of helicon SOL losses may be possible depending on the density gradient.

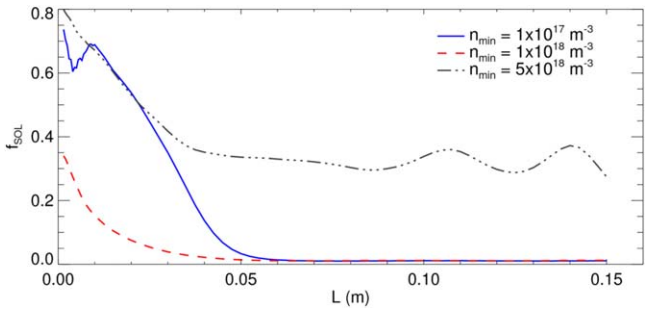

Figure 9. f_{SOL} is shown for $n_{\mathrm{min}} = 1 \times 10^{17}$, 1×10^{18}, and $5 \times 10^{18}\ \mathrm{m}^{-3}$ as a function of the density gradient ranging from 0 to 0.15 m. Frequency = 476 MHz, $\mathrm{ant}_z = 0.45$ m, $\mathrm{ant}_\rho = 1.3$, $n_{||} = 3$, and $v_e/\omega = 0.01$ for this figure. n_{cutoff} is approximately $2.1 \times 10^{18}\ \mathrm{m}^{-3}$.

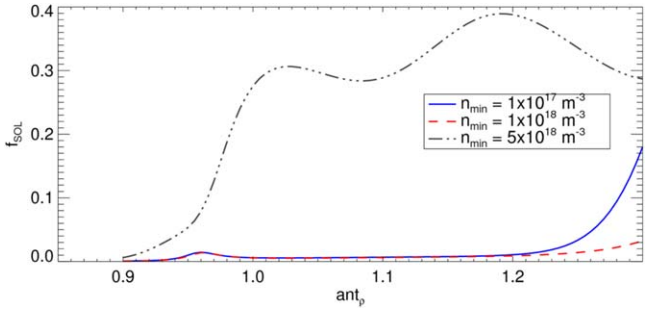

Figure 10. f_{SOL} is shown for $n_{\mathrm{min}} = 1 \times 10^{17}$, 1×10^{18}, and $5 \times 10^{18}\ \mathrm{m}^{-3}$ as a function of the radial location in toroidal flux coordinates. Frequency = 476 MHz, $L = 0.05$ m, $\mathrm{ant}_z = 0.45$ m, $n_{||} = 3$, and $v_e/\omega = 0.01$ for this figure.

5. Parametric scan of various antenna parameters

This section shows how the SOL losses can depend on various antenna parameters, such as the antenna radial location, antenna frequency, and antenna parallel wavelength. Besides being useful in understanding the importance of the helicon fast wave cutoff, these parameter scans also indicate possibilities of the effects of accessibility [12] and evanescent layer on antenna loading [33] and helicon SOL losses, which are shown in equations (10) and (11)

$$n_{||\mathrm{crit}} = \left[1 - \left(\frac{\omega^2}{\omega_{ce}\omega_{ci}}\right)\right]^{-1/2}, \tag{10}$$

$$R_L \propto \mathrm{e}^{-2\omega n\, x_{\mathrm{cutoff}}/c}, \tag{11}$$

where $n_{||\mathrm{crit}}$ is the critical $n_{||}$ for helicon wave accessibility, R_L is the antenna loading and x_{cutoff} is the distance from the antenna to the helicon fast wave cutoff layer. A value of $n_{||}$ near the accessibility limit implies that more power is deposited to the edge and possibly the SOL. For an antenna frequency at 476 MHz, $n_{||\mathrm{crit}} = 2.1$. It will be shown that a decreased antenna loading appears correlated to a higher helicon SOL loss. To estimate x_{cutoff}, the cutoff density is needed. The dependence of the cutoff density on various parameters is shown in equation (9). A higher cutoff density implies a thicker evanescent zone, and a lower antenna loading.

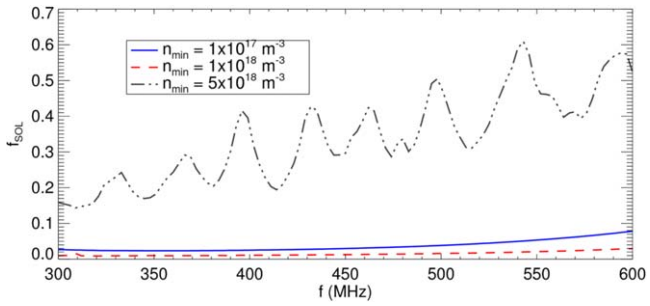

Figure 11. f_{SOL} is shown for $n_{\mathrm{min}} = 1 \times 10^{17}$, 1×10^{18}, and $5 \times 10^{18}\ \mathrm{m}^{-3}$ as a function of the antenna frequency ranging from 300 to 600 MHz. $L = 0.05$ m, $\mathrm{ant}_z = 0.45$ m, $\mathrm{ant}_\rho = 1.3$, $n_{||} = 3$, and $v_e/\omega = 0.01$ for this figure.

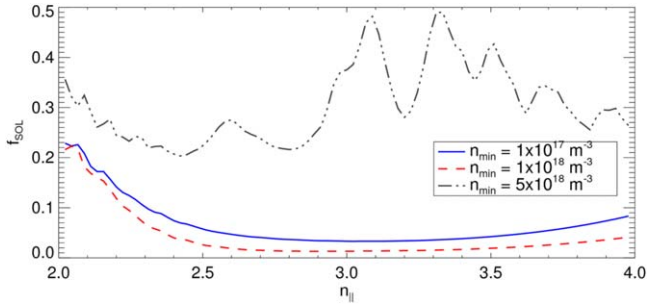

Figure 12. f_{SOL} is shown for $n_{\mathrm{min}} = 1 \times 10^{17}$, 1×10^{18}, and $5 \times 10^{18}\ \mathrm{m}^{-3}$ as a function of $n_{||}$ from 2 to 4. $L = 0.05$ m, $\mathrm{ant}_z = 0.45$ m, $\mathrm{ant}_\rho = 1.3$, frequency = 476 MHz and $v_e/\omega = 0.01$ for this figure.

Figure 10 shows f_{SOL} as a function of antenna radial location for three different n_{min}. For the highest n_{min}, as shown in figure 2, there are strong $|E|$ field structures, which causes much higher f_{SOL} relative to lower n_{min}. The trend with antenna location appears to be on average increasing with antenna radial distance from the LCFS. For n_{min} such that a cutoff layer exists, f_{SOL} is very low, except for the antenna locations at larger radius where it strongly increases. This is consistent with increasing x_{cutoff} for increasing antenna radial location as the cutoff density is at the same location and the antenna radial distance moves radially outwards. At the antenna locations furthest out radially, f_{SOL} is also largest for the smallest n_{min}, consistent with antenna loading.

Figure 11 shows f_{SOL} as a function of antenna frequency for three different n_{min}. For all three n_{min}, there is on average an increasing trend of f_{SOL} with increasing antenna frequency. This may possibly be correlated with antenna loading; the cutoff density is proportional to the frequency, so at higher frequency, the distance to cutoff increases and therefore the loading decreases. The SOL loss increases accordingly. For the highest $n_{\mathrm{min}} = 5 \times 10^{18}\ \mathrm{m}^{-3}$, f_{SOL} shows periodic behavior that is consistent with the strong $|E|$ field structures shown in figure 2. For $n_{\mathrm{min}} = 1 \times 10^{17}$ or $1 \times 10^{18}\ \mathrm{m}^{-3}$, f_{SOL} is much lower and shows no periodic behavior with frequency. For the 476 MHz frequency used on DIII-D, f_{SOL} appears to be only a few percent.

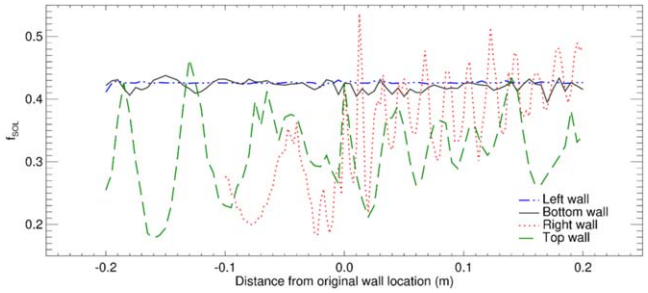

Figure 13. f_{SOL} is calculated by shifting each of the four walls of the rectangular boundary by up to ± 0.2 m while leaving the other three walls the same. Variations in the left wall (blue dotted–dashed line), bottom wall (black solid line), right wall (red short-dashed line) and top wall (green long-dashed line) are shown. $L = 0.05$ m, $\text{ant}_z = 0.45$ m, $\text{ant}_\rho = 1.3$, $n_{\min} = 5 \times 10^{18}\,\text{m}^{-3}$, frequency $= 476$ MHz and $\upsilon_e/\omega = 0.01$ for this figure.

Figure 12 shows f_{SOL} as a function of $n_{||}$ for three different $n_{\min}$. For $n_{\min} = 5 \times 10^{18}\,\text{m}^{-3}$, there are again strong $|E|$ field structures, which causes much higher f_{SOL} relative to lower $n_{\min}$. For $n_{\min} = 1 \times 10^{17}$ or $1 \times 10^{18}\,\text{m}^{-3}$, f_{SOL} is relatively low ranging from approximately 20% for $n_{||} = 2$ to approximately 5% for $n_{||} = 4$. f_{SOL} increases at both low and high $n_{||}$. For high $n_{||}$, this is correlated with antenna loading, as antenna loading decreases for increasing $n_{||}$. For low $n_{||}$, this is possibly due to helicon wave accessibility, as $n_{||}$ is approaching $n_{||\text{crit}} = 2.1$. The helicon wave starts to be damped strongly in the edge and SOL, leading to a significantly higher f_{SOL}. This SOL loss supports then design choice of $n_{||} = 3$ for the DIII-D helicon antenna [12].

6. FEM in different tokamak vacuum vessel geometry

The simulations in sections 4 and 5 assume a rectangular vacuum vessel boundary. The goal of this section is to understand how the helicon SOL losses are affected by poloidal variations in the vacuum vessel geometry. 2D axisymmetric geometry does not allow toroidal variations in the geometry, so this paper cannot address private limiters, antenna limiters, or a grounded antenna box. The results of the model could therefore be very different with more realistic antenna geometry, but this is outside the scope of this paper.

The simplest test of the poloidal variation of the vacuum vessel geometry is to modify the location of each of the four walls of the rectangular boundary separately while leaving the location of the other three walls the same. This is shown in figure 13 for $n_{\min} = 5 \times 10^{18}\,\text{m}^{-3}$ where f_{SOL} is calculated by shifting the left wall (blue dotted–dashed line), bottom wall (black solid line), right wall (red short-dashed line) and top wall (green long-dashed line) by up to ± 0.2 m while the other three walls are fixed. When only the left or bottom wall position is varied, f_{SOL} varies only a few percent. The change in f_{SOL} when the location of the left (high-field-side) wall is modified is particularly small. When the right or top wall is varied, however, f_{SOL} can change significantly, on the order of 20%. This is likely because the electric fields $|E|$ in the SOL, as shown in figures 2(c) and (d), are high near the top and right wall where the antenna is located. The helicon $|E|$ field near the bottom wall and particularly the left wall is much lower.

One of the greatest advantages of using a finite element code is that it permits the study of complicated geometry. In figure 14, the helicon $|E|$ field is calculated for different vacuum vessel geometries at $n_{\min} = 5 \times 10^{18}\,\text{m}^{-3}$. Figure 14(a) is the rectangular boundary that has been used in sections 4 and 5 of this paper, figure 14(b) is the vacuum vessel geometry for DIII-D from approximately 1997–2009, figure 14(c) is the vacuum vessel geometry for DIII-D from approximately 2010–2014, and figure 14(d) is the vacuum vessel geometry for DIII-D currently. It can be observed that the vacuum vessel geometry can qualitatively change the SOL $|E|$ field patterns.

A more quantitative calculation of f_{SOL} is shown for a range of $n_{\min}$ at these four different vacuum vessel geometries in figure 15. In all four cases, f_{SOL} increases substantially when $n_{\min}$ is greater than the helicon wave cutoff density. f_{SOL} can vary significantly depending on the vacuum vessel geometry. This is especially noticeable when $n_{\min}$ is greater than the helicon wave cutoff density, although some differences do occur even when $n_{\min}$ is less than the helicon wave cutoff density. The losses for the rectangular boundary are larger for the rectangular boundary when $n_{\min} > n_{\text{cutoff}}$. This is again likely because of the increased area in the SOL with high $|E|$. When $n_{\min} < n_{\text{cutoff}}$, the losses are small in the few percent range for this collision frequency.

While not shown, a coarse scan of the dependence of f_{SOL} with antenna and plasma parameters in the realistic geometry indicate similar trends to those observed in sections 4 and 5.

7. Discussion and conclusions

A reduced FEM that can reproduce the trends of a full wave hot plasma AORSA simulation has been developed to more extensively study helicon wave power losses in the SOL as a function of various important parameters. Through this computational study, the importance of different physical mechanisms (antenna loading, wave accessibility, SOL wave structures) has been assessed as loss mechanisms in the simulation. The computational study also identified important parameters, such as the minimum density being larger or smaller than the helicon fast wave cutoff density, distance from the cutoff layer to the antenna, as well as the parallel wavenumber accessibility criterion. Other factors such as vacuum vessel geometry was also considered and seem to be important only when there are significant SOL wave structures.

The computational study highlights potential optimization scenarios for future experiments. There is an optimal minimum SOL density to reduce helicon losses. If the minimum SOL density is too high, large-amplitude wave structures form in the SOL. If the minimum SOL density is too low, antenna loading can be an issue. Reducing SOL loss

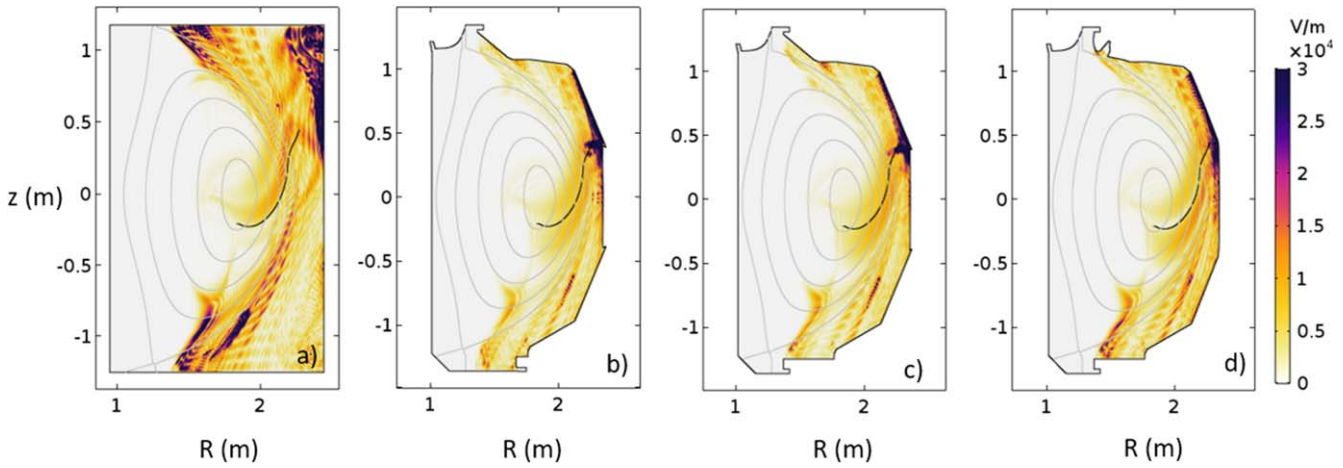

Figure 14. $|E|$ image plots of simulation at different vacuum vessel geometries at $L = 0.05$ m, $\text{ant}_z = 0.45$ m, $\text{ant}_\rho = 1.3$, $n_{\min} = 5 \times 10^{18}$ m^{-3}, frequency $= 476$ MHz and $\upsilon_e/\omega = 0.01$ for this figure.

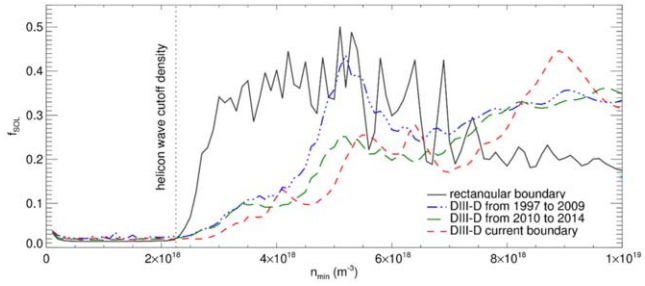

Figure 15. f_{SOL} is shown for a range of $n_{\min}$ at these four different vacuum vessel geometries for $L = 0.05$ m, $\text{ant}_z = 0.45$ m, $\text{ant}_\rho = 1.3$, frequency $= 476$ MHz, $n_{||} = 3$, and $\upsilon_e/\omega = 0.01$ for this figure.

mechanisms (ν/ω) will be desirable. ν/ω is currently a proxy for realistic SOL loss mechanisms, and a more realistic physical mechanism for SOL loss is needed for further optimization.

Acknowledgments

Thanks to David Green (ORNL) and R I Pinsker (General Atomics) for discussion. This work was supported by US Department of Energy, Office of Science, Office of Fusion Energy Sciences under contract numbers DE-AC05-00OR22725, DE-AC02-09CH11466. This manuscript was authored by UT-Battelle, LLC, under Contract No. DE-AC05-00OR22725 with the US Department of Energy. The US Government retains and the publisher, by accepting the article for publication, acknowledges that the US Government retains a non-exclusive, paid-up, irrevocable, world-wide license to publish or reproduce the published form of this manuscript, or allow others to do so, for US Government purposes. The Department of Energy will provide public access to these results of federally sponsored research in accordance with the DOE Public Access Plan (http://energy.gov/downloads/doe-public-access-plan).

ORCID iDs

C Lau https://orcid.org/0000-0002-8576-5867

References

[1] Najmabadi F *et al* 1991 The ARIES-I tokamak reactor study *Fusion Technol.* **19** 783–90
[2] Najmabadi F *et al* 1997 Overview of the ARIES-RS reversed-shear tokamak power plant study *Fusion Eng. Des.* **38** 3–25
[3] Najmabadi F *et al* 2006 The ARIES-AT advanced tokamak, advanced technology fusion power plant *Fusion Eng. Des.* **80** 3–23
[4] Maisonnier D *et al* 2005 The European power plant conceptual study *Fusion Eng. Des.* **75–79** 1173–9
[5] Maisonnier D *et al* 2007 Power plant conceptual studies in Europe *Nucl. Fusion* **47** 1524–32
[6] Kikuchi M 1990 Steady state tokamak reactor based on the bootstrap current *Nucl. Fusion* **30** 265–76
[7] Konishi S, Nishio S and Tobita K 2002 DEMO plant design beyond ITER *Fusion Eng. Des.* **63–64** 11–7
[8] Tobita K *et al* 2009 Compact DEMO, SlimCS: design progress and issues *Nucl. Fusion* **49** 075029
[9] Zohm H *et al* 2013 On the physics guidelines for a tokamak DEMO *Nucl. Fusion* **53** 073019
[10] Sorbom B N *et al* 2015 ARC: a compact, high-field, fusion nuclear science facility and demonstration power plant with demountable magnets *Fusion Eng. Des.* **100** 378–405
[11] Vdovin V L 2013 Current generation by helicons and lower hybrid waves in modern tokamaks and reactors ITER and DEMO. Scenarios, modeling and antennae *Plasma Phys. Rep.* **39** 95–119
[12] Prater R *et al* 2014 Application of very high harmonic fast waves for off-axis current drive in the DIII-D and FNSF-AT tokamaks *Nucl. Fusion* **54** 083024
[13] Jaeger E F, Berry L A, D'Azevedo E, Batchelor D B and Carter M D 2001 All-orders spectral calculation of radio-frequency heating in two-dimensional toroidal plasmas *Phys. Plasmas* **8** 1573–83
[14] Lau C *et al* 2018 AORSA full wave calculations of helicon waves in DIII-D and ITER *Nucl. Fusion* **58** 066004
[15] Bertelli N *et al* 2015 Effect of the scrape-off layer in AORSA full wave simulations of fast wave minority, mid/high

harmonic, and helicon heating regimes *AIP Conf. Proc.* **1689** 30010
[16] Chen F F 1991 Plasma ionization by helicon waves *Plasma Phys. Control. Fusion* **33** 339–64
[17] AB COMSOL 2012 COMSOL Multiphysics User Guide http://people.ee.ethz.ch/~fieldcom/pps-comsol/documents/User%20Guide/COMSOLMultiphysicsUsersGuide.pdf
[18] Garrett M L and Wukitch S J 2012 Mitigation of radio frequency sheaths through magnetic field-aligned ICRF antenna design *Fusion Eng. Des.* **87** 1570–5
[19] Jacquot J *et al* 2013 2D and 3D modeling of wave propagation in cold magnetized plasma near the Tore Supra ICRH antenna relying on the perfectly matched layer technique *Plasma Phys. Control. Fusion* **55** 115004
[20] Lu L *et al* 2016 Ion cyclotron wave coupling in the magnetized plasma edge of tokamaks: impact of a finite, inhomogeneous density inside the antenna box *Plasma Phys. Control. Fusion* **58** 055001
[21] Meneghini O *et al* 2011 SOL effects on LH wave coupling and current drive performance on alcator C-Mod *AIP Conf. Proc.* **1406** 411–8
[22] Takase Y *et al* 2011 Development of a plasma current ramp-up technique for spherical tokamaks by the lower hybrid wave *Nucl. Fusion* **51** 063017
[23] Preynas M *et al* 2013 Experimental characterization and modelling of non-linear coupling of the lower hybrid current drive power on tore supra *Nucl. Fusion* **53** 013012
[24] Stix T H 1992 *Waves in plasmas* (New York : Am. Inst. Physics)
[25] Ono M 1995 High harmonic fast waves in high beta plasmas *Phys. Plasmas* **2** 4075–82
[26] Lau C *et al* 2015 Using AORSA to simulate helicon waves in DIII-D *AIP Conf. Proc.* **1689** 080011
[27] Smirnov A P N T 1994 *Bull. Am. Phys. Soc.* **39** 1626
[28] Bertelli N *et al* 2016 Full wave simulations of fast wave efficiency and power losses in the scrape-off layer of tokamak plasmas in mid/high harmonic and minority heating regimes *Nucl. Fusion* **56** 016019
[29] Bertelli N *et al* 2014 Full wave simulations of fast wave heating losses in the scrape-off layer of NSTX and NSTX-U *Nucl. Fusion* **54** 083004
[30] Rudakov D L *et al* 2005 Far scrape-off layer and near wall plasma studies in DIII-D *J. Nucl. Mater.* **337–339** 717–21
[31] Green D L *et al* 2011 Predicting high harmonic ion cyclotron heating efficiency in tokamak plasmas *Phys. Rev. Lett.* **107** 145001
[32] Perkins R J, Hosea J C, Bertelli N, Taylor G and Wilson J R 2016 Resonance in fast-wave amplitude in the periphery of cylindrical plasmas and application to edge losses of wave heating power in tokamaks *Phys. Plasmas* **23** 070702
[33] Parisot A *et al* 2004 ICRF loading studies on alcator C-Mod *Plasma Phys. Control. Fusion* **46** 1781–92